IOP Publishing Quantum Sci. Technol. 10 (2025) 045006 https://doi.org/10.1088/2058-9565/adf2d6

Quantum Science and Technology

OPEN ACCESS

RECEIVED
24 May 2025

REVISED
2 July 2025

ACCEPTED FOR PUBLICATION
22 July 2025

PUBLISHED
5 August 2025

PAPER

Readout of strongly coupled NV center-pair spin states with deep neural networks

Matthew Joliffe[1], **Vadim Vorobyov**[1,*] **and Jörg Wrachtrup**[1,2]

[1] 3rd Institute of Physics, IQST, and Research Center SCoPE, University of Stuttgart, Stuttgart, Germany
[2] Max Planck Institute for Solid State Physics, Stuttgart, Germany
[*] Author to whom any correspondence should be addressed.

E-mail: v.vorobyov@pi3.uni-stuttgart.de

Keywords: measurement, quantum sensing, NV center, color center, machine learning, spin qubit

Abstract

Optically addressable electron spin clusters are of interest for quantum computation, simulation and sensing. However, with interaction length scales of a few tens of nanometers in the strong coupling regime, they are unresolved in conventional confocal microscopy, making individual readout problematic. Here we show that when using a single shot readout technique, collective states of the combined register space become accessible. By using spin to charge conversion of the defects we draw the connection between the intricate photon count statistics with spin state readout using deep neural networks. This approach is particularly versatile with further scaling the number of constituent spins in a cluster due to complexity of the analytical treatment. We perform a proof of concept measurement of the correlated classical signal, paving the way for using our technique in realistic applications.

1. Introduction

Spin defects in solids have emerged as promising quantum systems which serve as versatile and powerful test models for numerous quantum applications [1]. Among recent demonstrations, quantum simulations of spin Hamiltonians [2], building of quantum registers [3, 4], and distributed [5–7] and entanglement enhanced [8] quantum sensing showcase the usage of multiple single color centers as a multipartite quantum sensor. Additionally, recent advances in material fabrication and controlled defect creation [9, 10] facilitate the extension of the platform beyond a single color center. One method to scale-up the local spin register is utilizing strongly coupled arrays of quantum dots, spin qubits, or color centers [11–16]. The necessity of strong coupling ($g \gg \Gamma_2$), where g is the coupling strength and Γ_2 is the decoherence, dictates emitters to be within distance $d \leqslant 20\,\mathrm{nm}$ ($g \geqslant 10\,\mathrm{kHz}$) and hence beyond the resolution of a conventional confocal microscopy ($\delta x > 300\,\mathrm{nm}$). This has the implication that readout couples to several systems at once, complicating the readout, which is a key prerequisite for operation of a spin register.

The techniques available for single defects in a confocal spot operation [17], nuclear [18], and electron spin [19, 20] readout could potentially be combined with super-resolution techniques, such as electrical assisted readout [21] with nanoscale contracts, optical super-resolution imaging [7, 22] or spectral multiplexing [6, 23] at low temperatures. However, most of these techniques cannot be broadly and flexibly applied to color centers. For example, the application of super-resolution and spectral demultiplexing techniques is limited when dealing with nanostructures, such as scanning probe diamond tips, due to spectral diffusion and broadening at low temperatures, as well as excitation beam distortions due complicated dielectric environment. Hence often, an efficient readout remains limited to a single nitrogen vacancy (NV) center per confocal spot [24, 25].

Here we explore an alternative method where we exploit the joint addressability of defects and harness the dynamics of their response signals. When multiple defects couple to the detection channel, a readout signal forms a multiplexed telegraph-like process, showing stochastic switching behavior between multiple discrete values. Upon calibration of a system's transition parameters, spin to charge conversion methods enable each

defect to be readout with high efficiency [17, 24, 26]. Spin to charge conversion at room temperature operates with a contrast similar to the population of the metastable singlet (MS) state. After the initial excitation and the calibration process, extracting the precise spin states requires multiple measurements. Recalibration due to parameters drifting and the growing complexity with increased number of defects make this cumbersome. In contrast, machine learning provides a viable approach to reading out a many qubit system. Here we perform spin to charge conversion combined with machine learning assisted statistical analysis for efficient readout of a diffraction unresolved spin cluster spaced by $d \sim 10$ nm. We perform a calibration of the readout using uncorrelated and correlated states. Our results pave the way towards correlation sensing and scalable quantum hardware based on dipolar coupled spin arrays of color centers.

2. Results

In our experiments we use an NV pair of multiple orientations created using the ion implantation reported in [27]. The NV pair system shown in figure 1(a). Is in the strong coupled regime $g \gg \Gamma_2$. The individual NVs are within the diffraction limited spot that makes individual readout a challenge. Our test system is comprised of two NV centers with two different crystal lattice orientations. The different orientations can therefore allow for individual addressability of the NV centers due to the different magnetic field alignment and hence transition frequencies. For example, optically detected magnetic resonance (ODMR) of the NV centers shows multiplexed signal corresponding to each of the NV centers figure 1(b). A challenge of a full state readout is to assign the signal to individual centers and perform a readout of the spin correlations. Here we exploit the alignment of the excitation laser polarization along one of the optical dipoles of NV1 (see figure 1(c)). Consequently, we increase the emission intensity of the selected NV1 orientation and decrease the intensity of the other orientation for NV2. This provides a way to create distinguishability between the two emitters' brightness's which can be harnessed for demultiplexing the readout in a single shot readout setting, e.g. of the defect charge state. The NV center has two main charge states, NV^- and NV^0, with their zero phonon line emission at wavelengths of 637 nm and 575 nm, respectively. By choosing a wavelength between these values (∼594 nm), we can efficiently excite only the NV^- charge state. Figure 1(c) shows a continuous readout of the two NV system. As the system jumps between the four possible charge states, the intensity varies. Figure 1(d) shows a histogram of the photon counting statistics of many charge state readouts. Distinction of 4 peaks in the histogram signals contribution of two two-level systems contributing to the observation with four possible combined states: $NV_1^-\ NV_2^-$, $NV_1^0\ NV_2^0$, $NV_1^-\ NV_2^0$, $NV_1^0\ NV_2^-$. When the NV pair system has its charge state prepared with a short 520 nm pulse prior to the charge state estimation, the overall probability of having the useful double negative state increases, reaching ∼40% (figure 1(e)). To maximize the distinguishability of the histogram peaks, we apply the polarization alignment such that NV1 is roughly twice as bright as NV2. The distribution of each charge state is expected to be a Poisson distribution, but these are slightly altered due to the charge state often switching mid readout [17, 24].

Due to the significant probability of charge state switching during a measurement, care must be taken when trying to assign the initial charge state at the time of readout. To account for the intricate charge state dynamics in photon distributions, we adapt the photon counting distribution derived for a single emitter and assume independence of their charge state switching events and rates:

$$p(n,k_1,k_2) = \sum_{i=0}^{n} p_1(N=i,k_1)\, p_2(N=n-i,k_2)\,, \tag{1}$$

where the $p_i(N,k_1)$ photon counting probability distributions conditioned on initial state k, derived in [17, 24] for single emitters. Figure 2(a) shows the histogram of a measurement with continuous charge state readout. The model equation (1) is able to fit the obtained distribution. As the model depends on the intrinsic charge switching and photon emission rates, after performing a series of measurements at various laser intensities we estimated the ionization and recombination rates versus the applied 594 nm laser illumination (figure 2(b)). This allows for the laser power and readout time to be optimized numerically for further readout use [17].

Next we use the ability to efficiently estimate the charge state and individual microwave control of the two NV centers to realize an efficient individual spin readout. To this end we map the spin of the centers to a long lived charge state. At room temperature, we cannot selectively ionize the spin states directly but we can use the meta stable state to achieve this. The MS state provides protection from the defect getting ionized figure 2(c) This, along with the differential decay probabilities through the MS, we can ionize to the NV^0 state. The full protocol runs as following. A short 594 nm laser excitation pulse excites both spin states. The $m_s = 0$ state is spin conserving and will cycle between the 0 ground and excited states. The $m_s = 1$ state has a

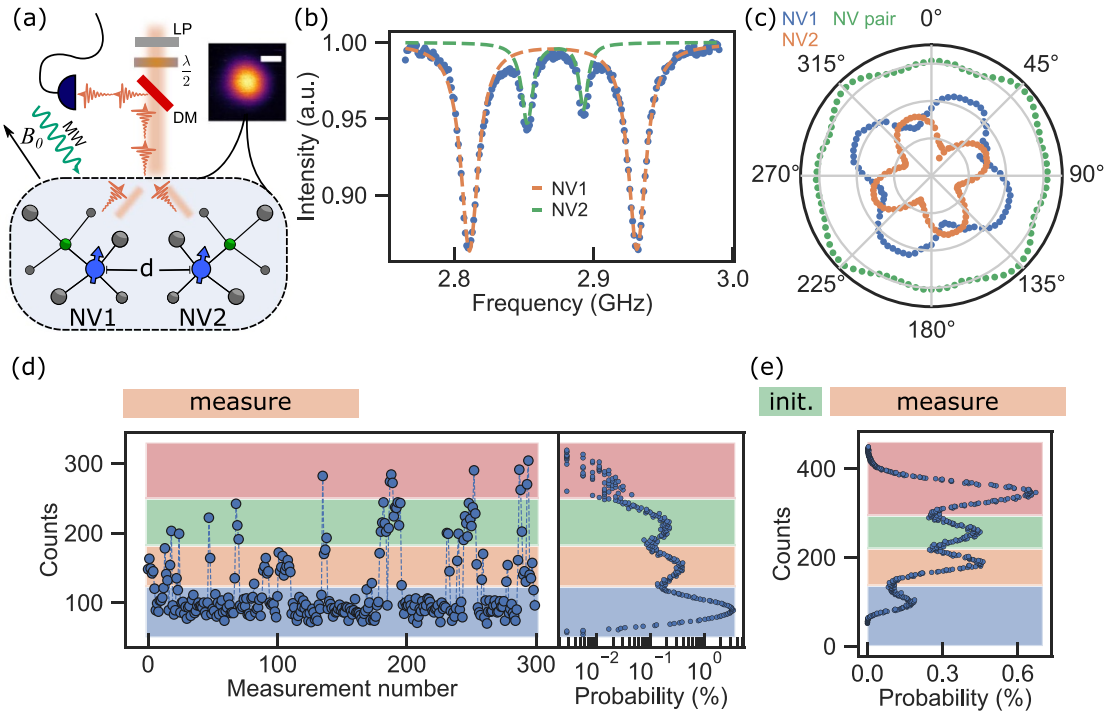

Figure 1. Charge state readout of the nitrogen vacancy (NV) pair system. (a) Schematic image of a differently oriented NV pair addressed with a confocal microscope. White bar on the confocal image is 200 nm in length. NV centers addressed with optical illumination and microwave frequency. (b) Optically detected magnetic resonance of the NV-pair system. (c) Polarization intensity plot. Blue, orange—intensity of NVs of different orientation as the excitation laser polarization is rotated. Green—combined intensity of the NV pair. (d) Timetrace of photon countrate under continuous weak illumination with a 594 nm laser. (e) Histogram of timetrace of 594 readout with a short 520 nm laser for charge state initialization.

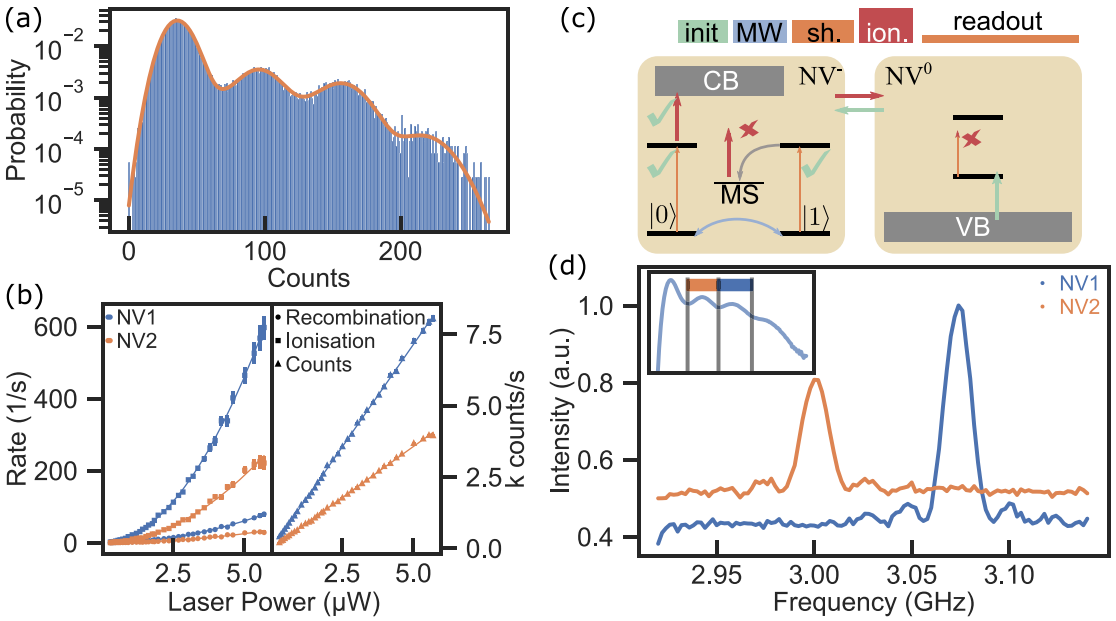

Figure 2. Charge switching dynamics of an NV pair and their spin to charge conversion for readout demultiplexing. (a) Histogram of counts of the NV pair under continuous 594 nm excitation. Fit with a two independent switching emitter model (see text). (b) Left—charge state switching rates as a function of laser power. Ionization is a two-photon process and thus increases quadratically with laser power. Right—emission intensity increases linearly in the low-power regime. (c) Schematic of the spin to charge conversion protocol. A 594 nm pulse cycles spin states between the ground and excited states. The spin 1 state has a significant probability of decaying through the MS state, where it is protected from a high power 638 nm pulse, while the spin 0 state is ionized with high probability. The charge state can then be read out with a lower power 594 nm pulse. The spin and charge state are then reset with a 520 nm pulse. (d) Demultiplexed readout of ODMR. A histogram is measured for each step of an ODMR measurement with spin to charge conversion (inset). The relative intensities of the middle two peaks are plotted as a function of probed frequency, and the two NV centers are read out individually and simultaneously.

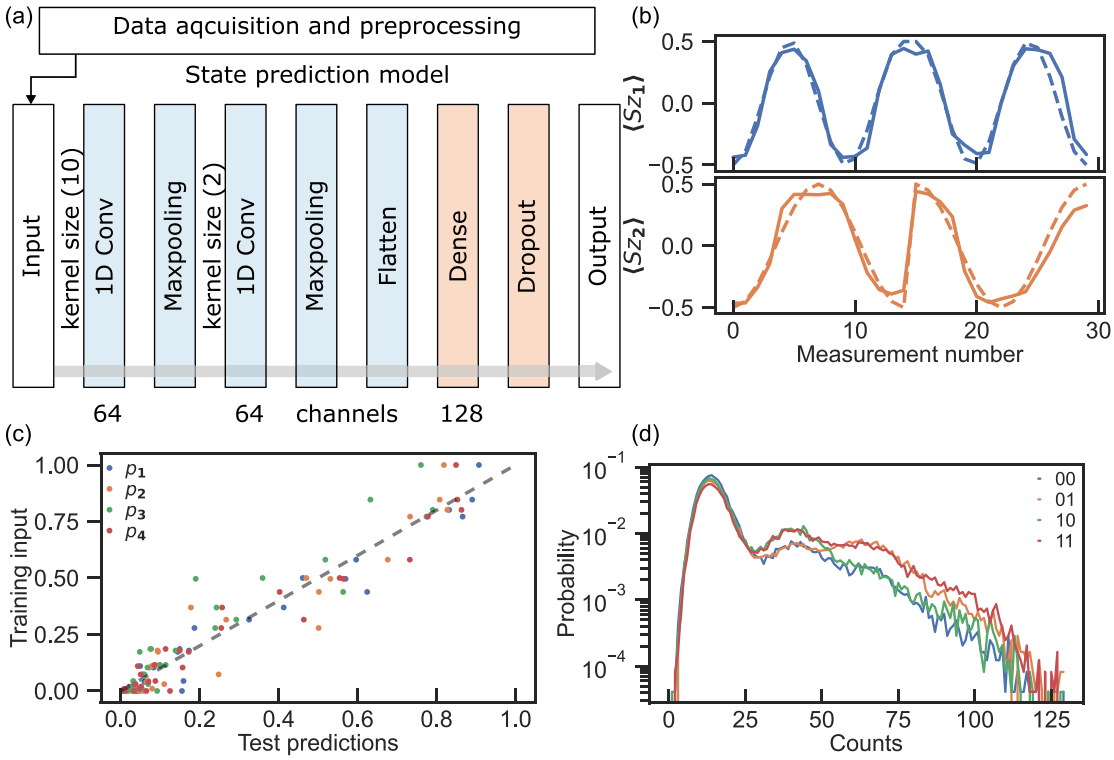

Figure 3. (a) Neural network model for robust state readout (a) overview of the model used in the experiment. (b) Known states are prepared and the corresponding histograms measured. These are fed into the ML model where features are extracted and the model attempts to learn relationships between the shape of the histogram and the probabilities it corresponds to. It then predicts the probabilities, and these are compared to the actual values. The model updates its internal weightings and continues this process trying to minimize the loss function between its predictions and the true values. The loss function used is the mean square error with an additional L2 regularization penalty that encourages lower weightings. (c) Comparison between the training data input and the predictions on the test set. The line $y = x$ represents perfect predictions (d) The photon counting histograms of the basis states for spin projections of individual NV centers correspondingly 00, 01, 10, 11.

significant probability of decaying through the long-lived MS state. A short intense 638 nm laser pulse will then ionize the $m_s = 0$ state, leaving the MS untouched. The probability of the $m_s = 1$ state being in the MS at the ionization pulse is 30%, similar to the ODMR contrast. The charge state can then be read out with a low power 594 nm laser pulse. Figure 2(d) demonstrates the combination of spin to charge conversion with charge state readout and individual spin control. A pulsed ODMR measurement is performed using spin to charge conversion and charge state readout. For each frequency in the measurement, a histogram is acquired (inset in the figure 2(d)). First we digitize and count the number of events in the second and third peaks of the histogram (inset). As the microwave frequency is swept, the occurrences of these events vary, representing effectively the spin flip probability for both NV centers in a demultiplexed manner. As this clearly shows the ability for individual spin readout, the quantitative analysis and calibration for precise readout of the defects is still cumbersome. This is due to complicated propagation dynamics of the spin states into the final charge state distribution and photon counting statistics, and depends significantly on such parameters as laser intensity, laser polarization and microscope alignment.

Additionally, the fitting method of the obtained photon statistics distribution for extraction of occupancies of the charge state is complicated due the large parameter space and numerical complexity of the model. This is also poorly scalable to systems with more than two emitters. Thus, here we find it natural to introduce a neural network based machine learning approach for reading out complex spin states with the model presented in figure 3(a). A normalized photon count histogram of a type shown in figure 2(a) is fed in as an input vector to the model. Following convolution and max-pooling layers are placed for feature extraction of the histograms. Fully connected dense layers placed afterwards are aimed at pattern learning and map the extracted features of the distributions to the probabilities of the initial states. An output layer yields model's estimation of the probabilities. During training, the predictions are compared to the actual values and the model updates its weightings using a gradient method. Using the `TensorFlow` python package [28], we were able to train a model to learn the spin states based on the photon histogram dataset at the inputs. To this end, known states are prepared via Rabi-like oscillations and a training histogram is measured for each state presented in figure 3(b). A separate test histogram is also measured for each of these states. After model training we perform cross-validation with the test dataset, which is shown in figure 3(c).

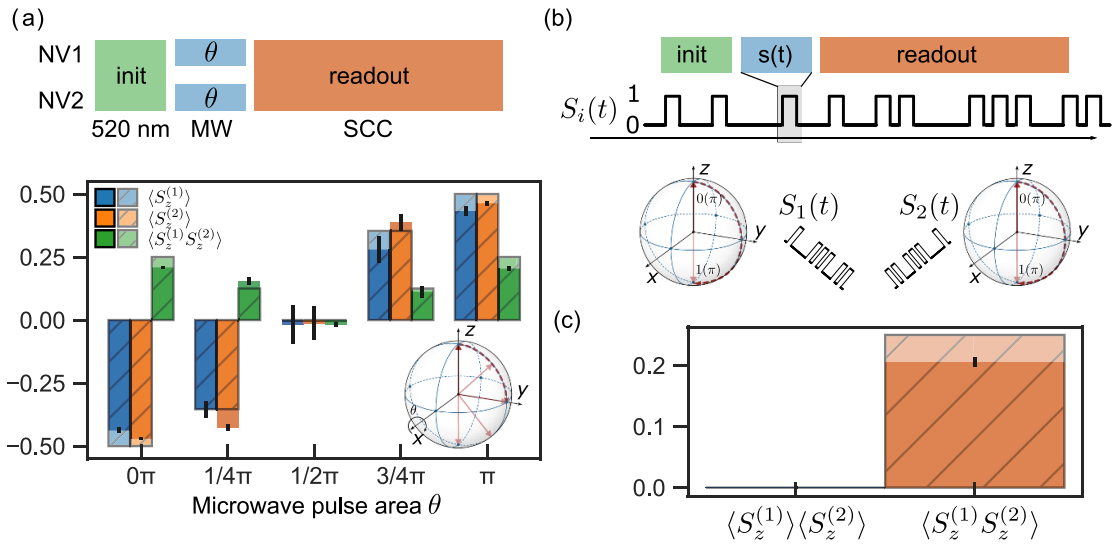

Figure 4. Readout of the spin pair states and sensing. (a) NV center pair prepared into the 00 state and then a fractional pulse is applied to both NVs and measured across many measurements. The histograms were fed into an already trained model and the expectation values obtained. (b) Quantum sensing of correlated zero mean signal with NV center signal. (c) Reconstructed product of single spins and correlation of the spin values due to correlated signal (noise).

It is important that the training and test data are kept separate to ensure that model does not overfit and its predictions can be generalized. Figure 3(d) shows the basis state histograms. It is evident that the histograms have a lot of overlap and a bias in the basis states representation, for example the first peak corresponding to the '00' charge state always has the predominant contribution to the signal. The features related to the differences between the states '0-', '-0' are related to exchange in the second and third peak height.

Having trained the model we apply it to perform accurate state readout and sensing using the NV center pair. Figure 4(a) shows the testing of the model on known states. Both NV center states are prepared in the negative charge with $m_s = 0$ state, then a rotation pulse with area $\theta = \{0, 1/4, 1/2, 3/4, 1\} \times \pi$ are applied to both NV centers. For each of the final states 64 histograms were measured and were fed into the model to get their spin probabilities. The predictions for the 64 measurements were averaged to obtain the plotted values with the standard deviation as the error. After that, the expectation values for the operators $\langle S_z^{(1)}\rangle$, $\langle S_z^{(2)}\rangle$ and $\langle S_z^{(1)} S_z^{(2)}\rangle$ were determined. As expected, the parity measurement $\langle S_z^{(1)} S_z^{(2)}\rangle$ stays positive for all of rotation angles, paving the way for efficient quantum sensing of correlations at the nanoscale. However, an interesting outcome is the result of the rotation to $\pi/2$ angle. It shows vanished correlations upon measurement in the S_z basis, even though the spins were prepared to the same state, due to the probabilistic nature of the projective measurements which erases the created correlation. Next we show the sensing of correlated signals. We perform a measurement where we apply simultaneously to both NVs correlated signal consisting of either an idle or an ideal π rotation mixed in random sequence. The figure 4(b) shows the schematic of the sequence execution applied for both sensors. The results of the measurements are shown in the figure 4(c). Since the individual responses $\langle S_z^{(1,2)}\rangle$ are $\pm 1/2$ upon $0(1)\pi$ pulses, the average expectation value of their product yields zero. The correlated signal, in turn, persists, yielding a way to separate the two [5].

3. Discussion

In this work we studied spin to charge assisted readout of electron spins of an NV center pair. However, this method could be extended to larger number of centers in a cluster. In figure 5 we show how the performance of the network scales with the number of defects. Interestingly, we found that for the network to distinguish between the individual spins, it is not necessary for them to differ in their fluorescence rates. It is sufficient that they have a distinct property, e.g. charge switching rates or fluorescence rates. This becomes crucial when the defects have same dipole orientation, as with increased number of defects, where some of them will inevitably have the same crystal orientation. We simulated photon statistics histogram produced by defect clusters of various sizes shown in figure 5(a). For three emitters, as demonstrated previously, we show the correlation plot in figure 5(b) and the simulated correlated sensing protocols in figure 5(c). However, with increasing cluster size, there are naturally less and less distinguishable properties of the emitters and the Pearson score for the networks drops close to 0 for a cluster of size 6, which shows the limits of the technique.

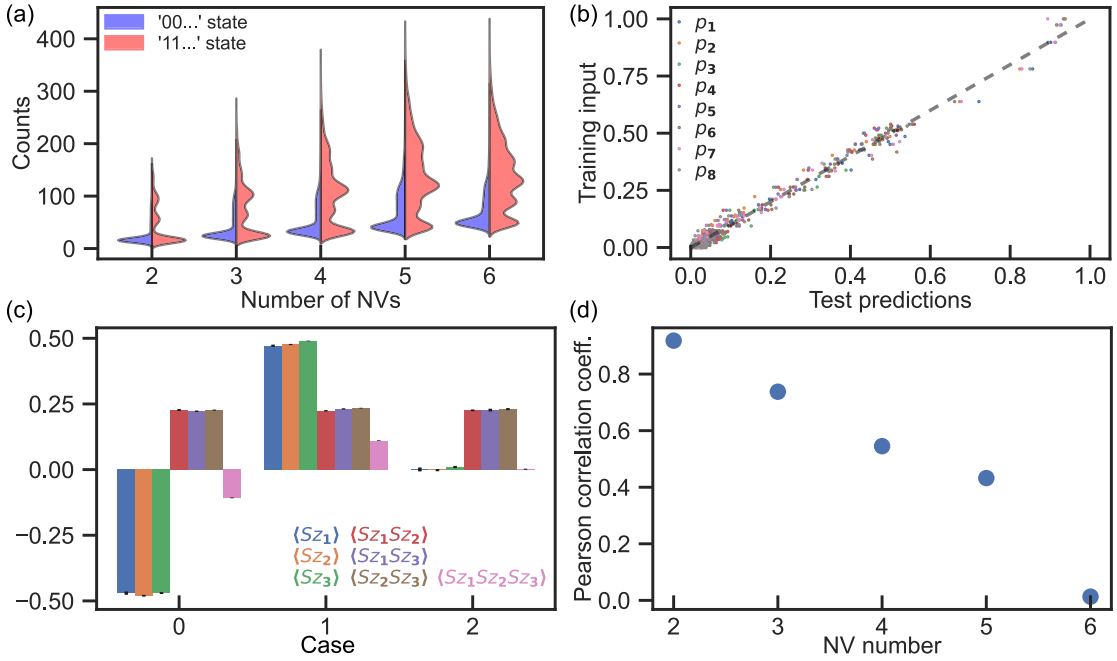

Figure 5. Scaling of the method to larger cluster sizes (numerical simulation). (a) Simulated photon histograms for various number of NV centers for $|000\ldots\rangle$ and $|111\ldots\rangle$ states (b) regression plot for training of the NN for an idealized three NV center system (c) state readout for three NV centers analogous to figure 4. Case '0' is pulse area $0 \cdot \pi$, '1' is $1 \cdot \pi$, and '2' is 50% statistical mixture of cases 0 and 1. (d) Scaling of Pearson coefficient for training of the model as a function of NV cluster size.

In conclusion, spin to charge conversion plus charge state readout allows for a novel way to read out two dipolar coupled NV centers simultaneously. Different orientations of NV centers within the diamond lattice allow for distinguishability via emission intensity which can be tuned with excitation polarization. As quantum systems get larger, readout becomes more challenging. Here we show machine learning is a viable way to readout systems consisting of multiple defects. A system of many emitters with switching charge states means significantly overlapping counts that would pose problems for traditional readout methods. Machine learning allows us to bypass the need to describe the system exactly by having the model learn the patterns that represent different spin states. Our method could be further applied for large clusters up to five systems. Applications to other technological platforms are straightforward. Due to the simplicity of the charge state readout, it could be straightforwardly applied to scanning probe setups, such as an NV-AFM [12]. Applications to quantum registers [16, 29], covariance magnetometry sensing [5], and quantum repeaters are within reach. For covariance magnetometry, as outlined in [5] the minimum covariance field scaling as $1/n_0$, instead of $1/\sqrt{n_0}$, where n_0 is a photon number from a single readout. Together with $\sqrt{N}$ convergence, this yields a 100 $\times$ speedup for utilization of spin to charge related techniques compared to conventional off resonant readouts. Furthermore, charge readout of spin clusters possess additional insights into preferentially aligned spin clusters, where the Zeeman shift yields a degenerate magnetic resonance spectrum. This technique could be further applied to a more general class of high fidelity readout, such as resonant readout, and repetitive readout. At the final stage of manuscript preparation we become aware of related works [6–8].

Data availability statement

All data that support the findings of this study are included within the article (and any supplementary files).

Acknowledgments

We acknowledge support from the European Commission through the QuantERA Project InQuRe (Grant Agreement Nos. 731473, and 101017733), the German ministry of education and research for the Project InQuRe (BMBF, Grant Agreement No. 16KIS1639K), support from the European Commission for the Quantum Technology Flagship Project QIA (Grant Agreement Nos. 101080128, and 101102140), the German ministry of education and research for the Project QR.X (BMBF, Grant Agreement No. 16KISQ013) and Baden-Württemberg Stiftung for the Project SPOC (Grant Agreement No. QT-6) and QC4BW as well as KQC4BW, Project Spinning (BMBF, Grant Agreement No. 13N16219) and the German Research Foundation (DFG, Grant Agreement No. GRK2642, FOR 2724).

Appendix A. NN training loss function

The machine learning model was created with TensorFlow 2.17.0 in Python 3.11.7. The model was structured such that it has an input layer that accepts data in the format of the histogram. The input layer feeds the data to a convolutional layer that extracts features from the histogram. The data is put into a max-pooling layer that reduces its spatial dimension, abstracting the data, and focuses on the most prominent features. From there the data goes into the dense layer that performs high level reasoning, learns to associate certain features and patterns with spin states. From there, the output layer makes a final prediction of the quantum state. The evolution of the training loss function is given in figure 6(a).

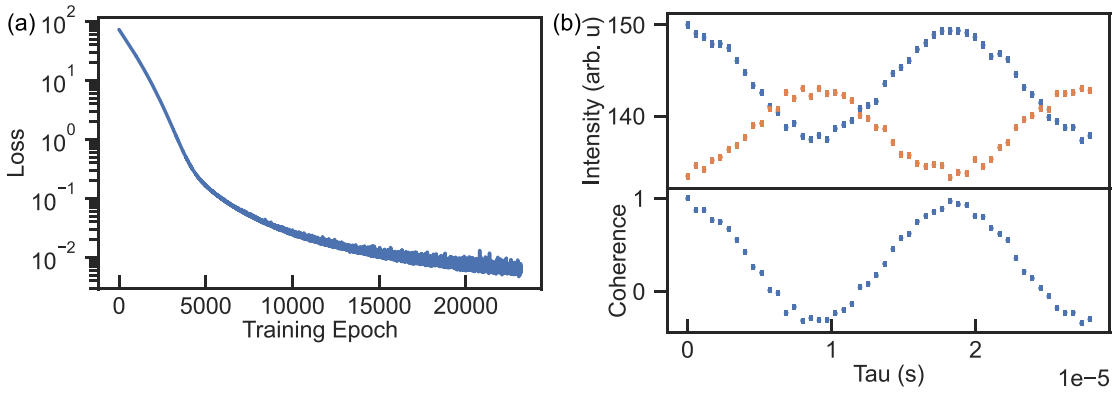

Figure 6. (a) Loss function evolution upon training of the model for the experimental case of NV center pair. (b) Double electron–electron resonance (DEER) NV-NV spectroscopy, revealing a $g \approx 2\pi \cdot 50$ kHz coupling strength between the two color centers.

Appendix B. Setup

The sample was implanted as in [27]. The proximity confirmed with dipolar interaction measurements to be within $d \sim 10$ nm ($g \approx 2\pi \cdot 50$ kHz) inferred from NV-NV DEER spectroscopy depicted on figure 6(b). Experiments were carried out with a home built confocal microscope. Homebuilt 520 nm green and 638 nm red diode lasers were combined with a 594 nm orange Huebner photonics Cobolt Mambo laser by coupling them into the same polarization maintaining Thorlabs P5-405BPM-FC-2 fibre. The polarization of all three lasers was set after outcoupling with Thorlabs LPVISC100 linear polarizer, WPQ10M-588 quarter wave plate, WPH10M-588 half wave plate mounted on Thorlabs KPRM1E/M rotational stage to control the direction of polarization. Keysight M8190A 12 GSa s^{-1} arbitrary waveform generator was used for MW pulses for NV spin control. Emitted photons detected with Perkin-Elmer SPCM-AQRH single photon counting device and counted with a TimeTagger 20. A PulseStreamer 8/2 was used for coordinating the three lasers, the AWG, and the TimeTagger.

Appendix C. Measurement parameters

Sequence element	Laser (nm)	Duration	Laser power
Initialization	520	3 μs	200 μW
MW sequence		ns to μs	
Spin excitation	594	50 ns	100 μW
Ionization	638	50 ns	30 mW
Readout	594	40 ms	700 nW

Appendix D. Neural network

```
import tensorflow as tf
from tensorflow import keras

class SparseLogging(tf.keras.callbacks.Callback):
    def __init__(self, print_every=10):
        super(SparseLogging, self).__init__()
        self.print_every = print_every

    def on_epoch_end(self, epoch, logs=None):
        if (epoch + 1) % self.print_every == 0:
            message = f"Epoch {epoch+1}: "
            for key, value in logs.items():
                message += f"{key} = {value:.4f}, "
            print(message.rstrip(", "))

sparse_logging = SparseLogging(print_every=200)

def NN(X_train, X_valid, y_train, y_test, num_nv):

    tf.keras.backend.clear_session()
    # Hyperparameter configurations
    init_lr = 1.8e-5
    decay_rate = 0.9
    decay_step = 1e4
    batch_size = 128
    dropout_rate = 0.2
    layer_size = 64
    l2_reg = 0.3
    dense_size = 128
    kernel_size = 10

    # Define learning rate schedule
    lr_schedule = tf.keras.optimizers.schedules.ExponentialDecay(
        initial_learning_rate=init_lr,
        decay_steps=decay_step,
        decay_rate=decay_rate,
        staircase=True)

    # Use the learning rate schedule in the optimizer
    optimizer = tf.keras.optimizers.Adam(learning_rate=lr_schedule)

    # Define the Neural Network Architecture
    model_histogram = keras.models.Sequential([
        keras.layers.Input(shape=(X_train.shape[1], 1)),
        keras.layers.Conv1D(filters=layer_size, kernel_size=kernel_size,
    activation="relu", padding="SAME"),
        keras.layers.MaxPooling1D(pool_size=2),
        keras.layers.Conv1D(filters=layer_size, kernel_size=2, activation="relu", padding=
    "SAME"),
        keras.layers.MaxPooling1D(pool_size=2),
        keras.layers.Flatten(),
        keras.layers.Dense(dense_size, activation="relu", kernel_regularizer=tf.keras.
    regularizers.l2(l2_reg)),
        keras.layers.Dropout(dropout_rate),
        keras.layers.Dense(2**num_nv, activation="softmax")])

    # Compile the model
    model_histogram.compile(optimizer=optimizer,
                    loss='mean_squared_error',
                    metrics=['mse'])

    # Early Stopping Callback

    early_stopping = keras.callbacks.EarlyStopping(
    monitor='val_loss',
    patience=500,
    restore_best_weights=True)

     # Train the model
    history = model_histogram.fit(
        X_train, y_train,
```

```
        epochs=40000,
        batch_size=batch_size,
        validation_data=(X_valid, y_valid),
        callbacks=[early_stopping, sparse_logging],
        verbose=0)
```

Appendix E. Sensitivity for covariance

The noise floor for covariance readout is $\sigma(\mathrm{Cov}) = \sigma_R^2/\sqrt{N}$. For the case of the photon flux with on average n_0 photons, the $\sigma_R^2 = n_0$ assuming an uncorrelated stationary Poisson distribution. Hence standard deviation of the photon count covariance is $n_0/\sqrt{N}$ (noise floor). Since each NVs fluorescence is modulated by the underlying stochastic magnetic field B_k through a factor like $\gamma B_k t$ with contrast C, the signal itself $\mathrm{Cov}(n_i, n_j) = \mathrm{Cov}(B_1 \cdot \gamma \cdot t \cdot B_2 \cdot \gamma \cdot t \cdot \pi \cdot \pi) \cdot C^2 \cdot n_0^2/4 = \mathrm{Cov}(B_1, B_2) \cdot (\gamma \cdot t \cdot \pi \cdot C \cdot n_0 \cdot 0.5)^2 = n_0/\sqrt{N}$. The minimally detected covariance signal hence $\delta\mathrm{Cov}(B, B) = n_0/\sqrt{N}/(g \cdot t \cdot \pi \cdot C \cdot \mathrm{e}^{-t/T2} \cdot n_0/2)^2$, where $N = T/(t + t_R)$ and finally the sensitivity is estimated as $\delta * \sqrt{T}$ to be $\eta_{\mathrm{cov}} \propto \frac{1}{n_0}\sqrt{t + t_R}/(\gamma t C \mathrm{e}^{-t/T_2})^2$.

Appendix F. Comparison of spin state readout methods

In this work we used three different approaches to spin state readout of the NV pair. In addition to the NN-based readout outlined in the main text, we also used mathematical fitting and photon counting approaches. The mathematical fitting used equation (1) to fit the charge state probabilities and then the spin states were calculated using measured initial charge state and SCC probabilities. This result was likely limited by large number parameters needed to fit the data. Four charge switching rates, four count rates, two initial charge state probabilities, and four SCC probabilities. The result was a Pearson correlation coefficient of 0.71 and a std of 0.25. The photon counting approach was an extension of the approach in figure 2(d) where photon number thresholds were used to try and count the number of occurrences of spin states. Charge state switching mid measurement made this infeasible. It had a Pearson correlation coefficient of 0.72 and std of 0.23. Both of these approaches were outperformed by the NN readout which had a Pearson correlation coefficient of 0.96 and std of 0.08.

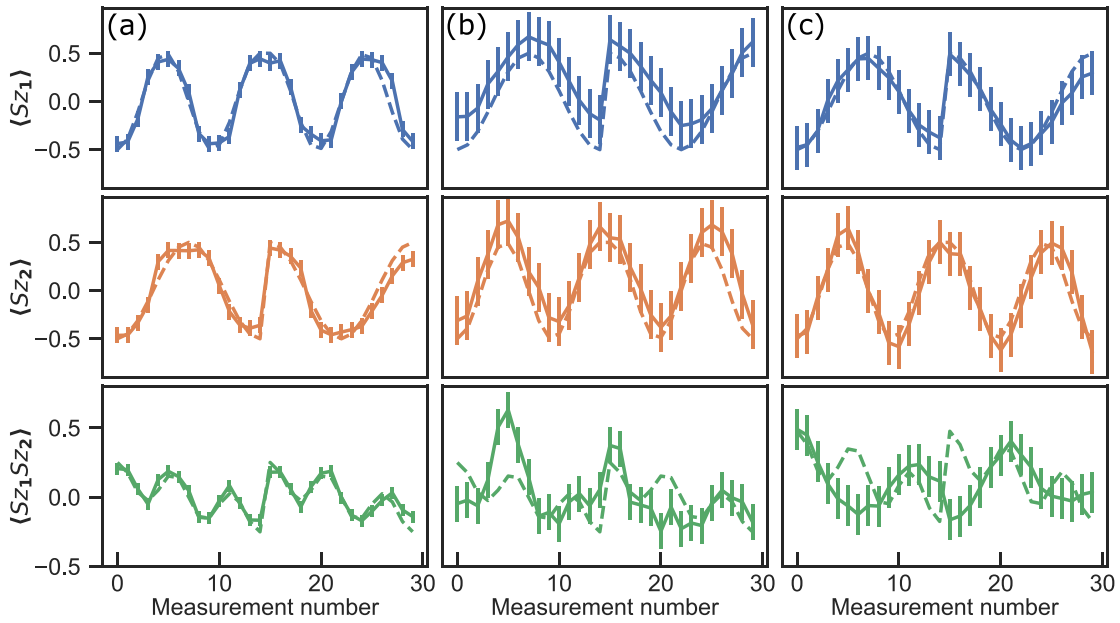

Figure 7. Comparison of spin readout methods in Rabi-like data. Dashed line—theory curve, solid line—experimental data with standard deviation. (a) Neural network model prediction. (b) Mathematical fitting based estimation. (c) Photon counting based estimation.

ORCID iD

Vadim Vorobyov 0000-0002-6784-4932

References

[1] Awschalom D D, Hanson R, Wrachtrup J and Zhou B B 2018 Quantum technologies with optically interfaced solid-state spins *Nat. Photon.* **12** 516
[2] Randall J, Bradley C, van der Gronden F, Galicia A, Abobeih M, Markham M, Twitchen D, Machado F, Yao N and Taminiau T 2021 Many-body–localized discrete time crystal with a programmable spin-based quantum simulator *Science* **374** 1474
[3] Bradley C E, Randall J, Abobeih M H, Berrevoets R C, Degen M J, Bakker M A, Markham M, Twitchen D J and Taminiau T H 2019 A ten-qubit solid-state spin register with quantum memory up to one minute *Phys. Rev. X* **9** 031045
[4] Vorobyov V, Zaiser S, Abt N, Meinel J, Dasari D, Neumann P and Wrachtrup J 2021 Quantum Fourier transform for nanoscale quantum sensing *npj Quantum Inf.* **7** 124
[5] Rovny J, Yuan Z, Fitzpatrick M, Abdalla A I, Futamura L, Fox C, Cambria M C, Kolkowitz S and de Leon N P 2022 Nanoscale covariance magnetometry with diamond quantum sensors *Science* **378** 1301
[6] Le X H, Dolgirev P E, Put P, Peterson E L, Pillai A, Zibrov A A, Demler E, Park H and Lukin M D 2025 Wideband covariance magnetometry below the diffraction limit (arXiv:2505.00260)
[7] Rovny J, Kolkowitz S and de Leon N P 2025 Multi-qubit nanoscale sensing with entanglement as a resource (arXiv:2504.12533)
[8] Zhou X *et al* 2025 Entanglement-enhanced nanoscale single-spin sensing (arXiv:2504.21715)
[9] Haruyama M *et al* 2019 Triple nitrogen-vacancy centre fabrication by $C_5N_4H_n$ ion implantation *Nat. Commun.* **10** 2664
[10] Ji W *et al* 2024 Correlated sensing with a solid-state quantum multisensor system for atomic-scale structural analysis *Nat. Photon.* **18** 230
[11] Broome M *et al* 2018 Two-electron spin correlations in precision placed donors in silicon *Nat. Commun.* **9** 980
[12] Huxter W S, Dalmagioni F and Degen C L 2024 Multiplexed scanning microscopy with dual-qubit spin sensors (arXiv:2407.19576)
[13] Oakes G *et al* 2023 Fast high-fidelity single-shot readout of spins in silicon using a single-electron box *Phys. Rev. X* **13** 011023
[14] Nurizzo M *et al* 2023 Complete readout of two-electron spin states in a double quantum dot *PRX Quantum* **4** 010329
[15] He Y, Gorman S, Keith D, Kranz L, Keizer J and Simmons M 2019 A two-qubit gate between phosphorus donor electrons in silicon *Nature* **571** 371
[16] Dolde F, Jakobi I, Naydenov B, Zhao N, Pezzagna S, Trautmann C, Meijer J, Neumann P, Jelezko F and Wrachtrup J 2013 Room-temperature entanglement between single defect spins in diamond *Nat. Phys.* **9** 139
[17] Zahedian M, Keller M, Kwon M, Javadzade J, Meinel J, Vorobyov V and Wrachtrup J 2023 On readout and initialisation fidelity by finite demolition single shot readout *Quantum Sci. Technol.* **9** 015023
[18] Neumann P, Beck J, Steiner M, Rempp F, Fedder H, Hemmer P R, Wrachtrup J and Jelezko F 2010 Single-shot readout of a single nuclear spin *Science* **329** 542
[19] Robledo L, Childress L, Bernien H, Hensen B, Alkemade P F and Hanson R 2011 High-fidelity projective read-out of a solid-state spin quantum register *Nature* **477** 574
[20] Rosenthal E I *et al* 2024 Single-shot readout and weak measurement of a tin-vacancy qubit in diamond *Phys. Rev. X* **14** 041008
[21] Siyushev P, Nesladek M, Bourgeois E, Gulka M, Hruby J, Yamamoto T, Trupke M, Teraji T, Isoya J and Jelezko F 2019 Photoelectrical imaging and coherent spin-state readout of single nitrogen-vacancy centers in diamond *Science* **363** 728
[22] Jaskula J-C, Bauch E, Arroyo-Camejo S, Lukin M D, Hell S W, Trifonov A S and Walsworth R L 2017 Superresolution optical magnetic imaging and spectroscopy using individual electronic spins in diamond *Opt. Express* **25** 11048
[23] Bersin E, Walsh M, Mouradian S L, Trusheim M E, Schröder T and Englund D 2019 Individual control and readout of qubits in a sub-diffraction volume *npj Quantum Inf.* **5** 38
[24] Shields B J, Unterreithmeier Q P, de Leon N P, Park H and Lukin M D 2015 Efficient readout of a single spin state in diamond via spin-to-charge conversion *Phys. Rev. Lett.* **114** 136402
[25] Zhang Q *et al* 2021 High-fidelity single-shot readout of single electron spin in diamond with spin-to-charge conversion *Nat. Commun.* **12** 1529
[26] Aslam N, Waldherr G, Neumann P, Jelezko F and Wrachtrup J 2013 Photo-induced ionization dynamics of the nitrogen vacancy defect in diamond investigated by single-shot charge state detection *New J. Phys.* **15** 013064
[27] Jakobi I, Momenzadeh S A, De Oliveira F F, Michl J, Ziem F, Schreck M, Neumann P, Denisenko A and Wrachtrup J 2016 Efficient creation of dipolar coupled nitrogen-vacancy spin qubits in diamond *J. Phys.: Conf. Ser.* **752** 012001
[28] Abadi M *et al* 2015 TensorFlow: large-scale machine learning on heterogeneous systems, software (available at: www.tensorflow.org/)
[29] Joas T *et al* 2024 High-fidelity electron spin gates in a scalable diamond quantum register (arXiv:2406.04199)